An Improvised Low Voltage Ride Through Technique for the Robust Power Control of PMSG Systems Feeding Weak Grid

[1]Amit Kumar, [2]Asha Rani M.A*

[1,2] Department of Electrical Engineering, National Institute of Technology Silchar, Fakirtilla, Assam (788014) India
[1]Mail-ID: amitkr_rs@ee.nits.ac.in, [2]Mail-ID:asharani@ee.nits.ac.in

Abstract
Grid-connected PMSGs exhibit significant sensitivity to unbalanced grid voltages, particularly during voltage sags, which introduce negative sequence components that lead to undesirable oscillations in grid currents, active/reactive power, and DC link voltage at twice the grid frequency. This study aims to enhance the dynamic performance of PMSGs under such adverse conditions by developing a novel reference current generation strategy that mitigates these fluctuations without relying on dual vector control. The approach estimates the stator flux angular frequency in the α–β frame using voltage and current signals, eliminating the need for a PLL or voltage differentiation. The MSC manages active power, while the GSC maintains constant DC link voltage and UPF. Extensive simulations and real-time validation using OPAL-RT OP4510 demonstrate the scheme's robustness. For instance, in Case I, oscillations in active power, reactive power, grid current, and DC voltage were reduced from 12.05%, 4.22%, 13.07%, and 0.422% to 0.497%, 1.73%, 7.37%, and 0.0152%, respectively. In Case IV with a severe phase-A fault, oscillations dropped from 86.56% to 12.32% in active power and from 87.23% to 32.23% in grid current. Across all test cases, total harmonic distortion in grid current was consistently brought below 5%, proving the method's superiority over conventional techniques. Simulations conducted on a 2.5kW PMSG under various unbalanced grid voltage conditions using PSCAD/EMTDC confirm the suggested method's efficacy and its edge over current control techniques.

Keywords: Rotor Angular Frequency, Sensitivity Analysis, S-PLL, Unbalanced Voltage, Vector Control.

Introduction
Currently, the globe is transitioning to green energy foundations, including wind, hydroelectricity, solar power, and tidal energy, in response to energy issues. Wind power is a form of green power that is clean and has garnered global interest. India has made substantial advancements in the capacity of renewable energy installations in the past year. In the year 2029-30, the current capacity derived from renewable energies (solar, wind, biomass, hydro, and radioactive) is expected to constitute around 64% of the overall installed capacity of 817,254 MW [2]. New energy output is being led by the fast advancement of the wind power generation technology. "Permanent Magnet Synchronous Generators (PMSGs), Squirrel Cage Induction Generators (SCIGs), Wound Rotor Induction Generators (WRIGs), and Doubly Fed Induction Generators (DFIGs)" are among the many generator types available for energy conversion. PMSG is predominant amongst them due to its outstanding efficiency, adaptable control, dependability, and changeable velocity range. The PMSG is directly linked to the grid via in succession conversion devices, eliminating the need for a gearbox; however, voltage sags resulting from an imbalanced grid may disrupt the stable operation of the conversion. An unbalance in the electrical grid will cause fluctuations in the DC link voltage, hence diminishing the lifespan of the DC link capacitance. It is necessary to regulate electricity at each stage of transfering via PMSG onto the grid such that one may achieve steady-state power transmission.
As MSC has no direct connection to the grid, it will exhibit reduced sensitivity to grid voltage imbalances. Nonetheless, a malfunction or significant imbalance in the grid inhibits the GSC from transferring power, resulting in a surge in DC link voltage and GSC currents, ultimately causing the breakdown of the GSC and capacitors. In a system with equilibrium, energy transfer through the MSC to the grid must be equivalent. The MSC exhibits minimal sensitivity to grid voltage fluctuations and continually provides electricity for distribution to the grid, regardless of grid disturbances. Furthermore, for grid-connected wind turbines functioning under dynamical conditions—such as variable wind velocities and system disruptions—precisely forecasting rotor speed and location becomes progressively intricate. Various sensorless estimation algorithms, both open-loop and closed-loop, have been explored [2]-[4]. In open-loop methods, precise system parameter measurements are crucial for accurately determining rotor speed and position. A common approach to estimating rotor speed involves differentiating the rotor position. Adaptive methods, including the "Sliding Mode Observer (SMO)" and the "Model Reference Adaptive System (MRAS)", were examined for calculating the stator EMF or flux through contrasting the settings of the PMSG with the reference model's [5]-[7]. A rotor angle measurement technique for PMSG-assisted WECS has been introduced, employing an adaptive low-pass filter in conjunction with a feedforward stabilizer [7]-[11]. Traditional control methods often struggle to maintain optimal performance under unbalanced grid voltage conditions [12]-[16]. A improved technique has been implemented to alleviate second harmonic DC bus voltage vibrations and torque distortion. This is accomplished by incorporating a compensating unit in parallel alongside the DC voltage in a PMSG network characterized by asymmetrical resistance [17].

The proposed technique reduces the necessity for supplementary electrical components and functions with markedly lower compensatory current. Moreover, research has investigated the utilization of external circuits, arranged in serial with the 3-phase windings, to rectify the off-balance impedance in asymmetrical 3 phase PMSGs [18]-[20]. Asymmetric impedance in a PMSG system arises from unbalanced resistances, self-inductances, and mutual inductances. A low-voltage ride-through strategy has been introduced in [21], where the "Machine-Side Converter (MSC)" manages the DC link voltage instead of the "Grid-Side Converter (GSC)". The nonlinear connection between generator rate and DC link value necessitates the inclusion of feedback linearization concept in the controller construct. To further improve efficiency in imbalanced situations, vector control using a twofold rotating coordinates frame is suggested in [24]. Because they are handled independently, positive and negative sequencing current elements must be distinguished in this method. This control approach is good at lowering active power output changes, but it doesn't do a very good job of limiting reactive power variations or high peak currents. Also covered in [25] is research on direct torque control (DTC) for drives of synchronous magnet motors. The electromagnetic force in a motor powered by a permanent magnet is shown to grow in relation to the angle along the flux connections between the stator and the rotating part, according to mathematical research. Because of this, a quick torque reaction is possible by modifying the stator flux linkage's rotational speed. Unfortunately, grid integration for PMSG is hindered by the increased ripples in machine characteristics that this strategy produces. A more dependable and efficient control framework for enhanced machine efficiency can be achieved by evaluating PMSG-based WECSs with both vector control as well as DTC. This shows the possibility to integrate important advantages of both systems. From [26] to [32]. immediate electricity components, such as a stable state, sinusoidal, and co-sinusoidal active and reactive energy, are the source of reference voltages in the event of grid instability. Minimizing frequency variations in grid active, grid currents and "direct current link voltage (DCLV)" are many control targets that are typically used to create GSC controller reference currents in the ways that have been published. Consequently, the control procedure is tricky and difficult to perform because standard double vector management for GSC required six PI processors.

This work introduces an innovative method for producing references current to regulate a PMSG amidst grid voltage imbalance, employing positively sequencing stator voltage and current elements within the static α-β reference frames. An enhanced stator flux computing approach is presented, obviating the necessity for a PLL. The suggested reference current incorporates an additional term to mitigate the impacts of imbalance. This method streamlines implementations by eliminating dual vector management, which otherwise causes temporal delays from sequential breakdown, adversely affecting the system's behavior. The MSC extracts active power from the device, whereas the GSC regulates a constant DCLV and facilitates current interchange with the grid at unity power factor (UPF). This approach's efficacy is confirmed by simulations on a 2.5kW PMSG utilizing "Power System Computer Aided Design/Electromagnetic Transients Including Direct Current (PSCAD/EMTDC)". The primary contribution of this research lies in proposing a novel reference current generation technique for PMSGs that effectively suppresses oscillations in power, grid current, and DCLV under unbalanced grid conditions. Unlike conventional methods, the approach eliminates the need for dual vector control or PLL, offering a unified and computationally efficient control strategy. The research is structured as follows: Section I introduces the problem and objectives. Section II covers the system modelling of the grid-connected PMSG. Section III details the proposed method for rotor speed estimation and reference current generation. Section IV analyzes the performance of the computed angular speed under parameter variations. The modeling results and discussions are presented in Section V, and the conclusion is provided in Section VI, this section summarizes the findings and emphasizes how effective the proposed control technique is.

System Modelling

A Wind Power Plant (WPP) based on a PMSG typically consists of five key components: the wind turbine, PMSG, MSC, GSC, and the grid [23]. For variable-speed, extensive-range, low-speed WPPs, a multi-pole synchronous generator is the preferred choice. In particular, PMSGs (Type-D WPPs) offer a broad operational speed range, reaching up to 2.5 times the rated speed. Through the use of consecutively converters, PMSGs are directly linked to the grid. The following part provides a comprehensive description of the system design.

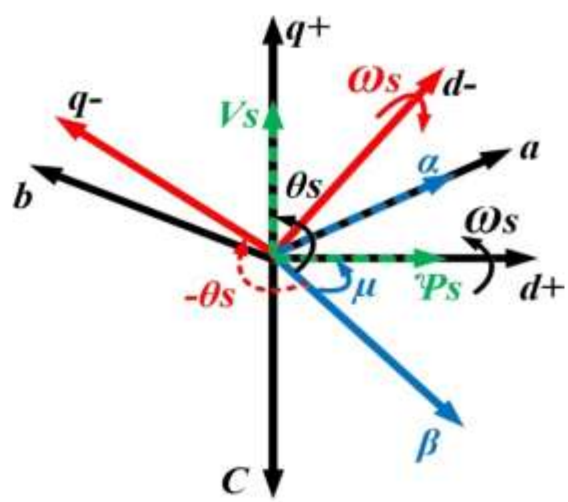

Fig. 1. Representation of Space Vectors.

A. MATHEMATICAL MODELING OF PMSG

Figure 1 shows the relationship between the levels and phases of important PMSG features. The stator's flux ϕsd is perpendicular to the d-axis, while the stator's voltage Vsq is pointed towards the q-axis.

In the stationary α-β references structure, the d-q reference frames rotates at the same angular velocity ω_{es} at every given time t, producing an angle θs=90+μ relative to the α-β frame [1].

Under the assumption that the PMSG's flux pattern is sinusoidal, the stator voltage V_s in the fixed α-β reference frames can be articulated as:

$$V_{s\alpha} = R_s i_{s\alpha} + \frac{d\varphi_{s\alpha}}{dt} \tag{1}$$

$$V_{s\beta} = R_s i_{s\beta} + \frac{d\varphi_{s\beta}}{dt} \tag{2}$$

Under equilibrium conditions, the rate for the shift of magnetic flux is zero. Therefore, the preceding phrases might be reformulated as:

$$V_{s\alpha} = R_s i_{s\alpha} + \omega_{es} L_{s\beta} i_{s\beta} \tag{3}$$

$$V_{s\beta} = R_s i_{s\beta} - \omega_{es} L_{s\alpha} i_{s\alpha} \tag{4}$$

Under the assumption of a sinusoidal flux dispersion in the PMSG, the stator voltage V_s in the d-q referenced frames can be articulated as:

$$V_{sd} = -\varphi_{sq}\omega_{es} + R_s i_{sd} + \frac{d\varphi_{sd}}{dt} \tag{5}$$

$$V_{sq} = \varphi_{sd}\omega_{es} + R_s i_{sq} + \frac{d\varphi_{sq}}{dt} \tag{6}$$

In a PMSG, flux is generated from two primary sources: the permanent magnets embedded in the rotor and the electric current flowing through the stator windings. These flux components link with the stator windings as:

$$\varphi_{sd} = L_{sd} i_{sd} + \varphi_{rd} \tag{7}$$

$$\varphi_{sq} = L_{sq} i_{sq} + \varphi_{rq} \tag{8}$$

The rotor magnetization is oriented along the d-axis, and in the absence of magnetic flux extending along the q-axis, the rotor flux may be expressed as:

$$\varphi_{rq} = 0, \qquad \varphi_{rd} = \varphi_{PM} \tag{9}$$

$$\varphi^*_{PM} = \varphi_{Sd} - L_{sd} i_{sd} \tag{10}$$

The PMSG torque can be expressed as:

$$T_e = \frac{3}{2} P_p \varphi_{PM} i_{sq} + \frac{3}{2} P_p (L_{sd} - L_{sq}) i_{sd} i_{sq} \tag{11}$$

Equation (11) has two terms: one for the magnetic and one for the reluctance torque. The inductances L_{sd} and L_{sd} are distinct in the scenario of a salient-pole system. The the inductances are the same nevertheless, for a machine without an identifiable pole [22]. Therefore, the torque expression can be rewritten as:

$$T_e = \frac{3}{2} P_p \varphi_{PM} i_{sq} \tag{12}$$

The PMSG system's mechanical properties can be characterized using the dynamical one-mass framework.

$$T_L = J\frac{d\omega_m}{dt} + B\omega_m + T_e \tag{13}$$

Here, *J* represents the inertia moment of the transmission system, while B denotes the coefficient of self-damping.

B. MODELING OF GSC AND DC LINK

The GSC and its control circuit are represented in the d-q reference frame by matching the grid voltage with the q-axis. There are extra sequence elements that show up with the +ve sequencing voltage when there is grid voltage imbalance. No zero-sequence voltages are taken into account in a 3-phase, wire system since the -ve sequence current does not have a circulating route. If the three-phase voltages are imbalanced, DSC can separate them into their respective +ve and -ve sequence voltage sections [3]. The voltages on the imbalanced grid in the a-b-c frame are represented by:

$$\begin{bmatrix} V_{ga} \\ V_{gb} \\ V_{gc} \end{bmatrix} = \begin{bmatrix} V_m^+ \sin(\omega_{eg}t) + V_m^p \sin(\omega_{eg}t) \\ V_m^+ \sin(\omega_{eg}t - 120^o) + V_m^p \sin(\omega_{eg}t - 120^o) \\ V_m^+ \sin(\omega_{eg}t - 240^o) + V_m^p \sin(\omega_{eg}t - 240^o) \end{bmatrix} \tag{14}$$

Here, V_m^p and V_m^+ show the voltage's both -ve and +ve components at, respectively, while ω_{eg} represents the angular frequency of the grid voltage.

Clarke's conversion enables the conversion of three-phase voltages into the α-β fixed coordinate framework as follows:

$$\begin{bmatrix} V_{g\alpha} \\ V_{g\beta} \end{bmatrix} = \frac{2}{3}\begin{bmatrix} 1 & -\frac{1}{2} & -\frac{1}{2} \\ 0 & \frac{\sqrt{3}}{2} & -\frac{\sqrt{3}}{2} \end{bmatrix}\begin{bmatrix} V_{ga} \\ V_{gb} \\ V_{gc} \end{bmatrix} = \begin{bmatrix} V_{g\alpha}^+ + V_{g\alpha-}^p \\ V_{g\beta}^+ + V_{g\beta-}^p \end{bmatrix}. \tag{15}$$

$$\begin{bmatrix} V_{g\alpha}^{+} \\ V_{g\beta}^{+} \\ V_{g\alpha-}^{p} \\ V_{g\beta-}^{p} \end{bmatrix} = \begin{bmatrix} V_{m}^{+} \sin(\omega_{eg} t) \\ -V_{m}^{+} \cos(\omega_{eg} t) \\ V_{m-}^{p} \sin(\omega_{eg} t) \\ V_{m-}^{p} \cos(\omega_{eg} t) \end{bmatrix} \quad (16)$$

The output active and reactive powers represented according to instantaneous power theory as

$$\begin{bmatrix} P_g \\ Q_g \end{bmatrix} = \frac{3}{2} \begin{bmatrix} V_{g\alpha} & V_{g\beta} \\ V_{g\beta} & -V_{g\alpha} \end{bmatrix} \begin{bmatrix} i_{g\alpha} \\ i_{g\beta} \end{bmatrix} \quad (17)$$

The DC connection maintains a steady power transmission from a generator to the grid in a balanced configuration. Nevertheless, whenever the system experiences an imbalance, variations in the electrical supply on the grid's side occur, which disturbs the consistent flow of power from the source to the grid. By factoring in the filter resistance R_f and inductance L_f, the voltage at the DC link and the d-q axis GSC voltages may be represented as

$$\frac{dV_{dc}}{dt} = \frac{i_c - i_L}{C} \quad (18)$$

$$V_{iod} = V_{gd} - R_f i_{gd} - L_f \frac{di_{gd}}{dt} + \omega_{eg} L_f i_{gq} \quad (19)$$

$$V_{ioq} = V_{gq} - R_f i_{gq} - L_f \frac{di_{gq}}{dt} + \omega_{eg} L_f i_{gd} \quad (20)$$

Equilibrium correction of the cross-coupling factors in eq (19) and (20) is required to get the d-q axis controlling voltage for GSC current management.

A Robust Reference Current Generation Using GSC For Improved LVRT Capability of PMSG

The prime objective of Gris Side Converter (GSC) control here is to minimize the oscilations in DC link voltage and to maintain UPF at the grid terminals. The presence of unbalance in grid side voltage leads to imbalanced and harmonically distorted currents at grid side which further leads to sustained oscillations at grid side parameters such as active power, ractive power and dc link voltage if not addressed/controlled. Let V_g represent the instantaneous grid voltage, which can be expressed as follows for a balanced grid:

$$V_g = V_{g\alpha} - jV_{g\beta} = (V_{gq} - jV_{gd})e^{j\mu} \quad (21)$$

When there is an imbalance in the grid, the voltage is shown as the total of both the +ve and -ve sequence component.

$$V_{gimb} = \left(V_{g\alpha}^{+} - V_{g\alpha-}^{p}\right) - j(V_{g\beta}^{+} - V_{g\beta-}^{p}) \quad (22)$$

Similarly, unstable currents can be expressed as the total of both series components, excluding zero-sequence factors due to the isolated neutrality position. Grid electricity, both reactive and active sides of a PMSG, articulated in relation to grid voltage and current components under balanced conditions, is delineated by equations (23) and (24). Nevertheless, in conditions of imbalanced voltage, they are expressed by equations (25) and (26).

$$P_g = \frac{3}{2}(V_{g\alpha} i_{g\alpha} + V_{g\beta} i_{g\beta}) \quad (23)$$

$$Q_g = \frac{3}{2}(V_{g\alpha} i_{g\beta} - V_{g\beta} i_{g\alpha}) \quad (24)$$

$$P_{gimb} = P_{ga} + P_{gb} + P_{gc} + P_{gd} \quad (25)$$

$$Q_{gimb} = Q_{ga} + Q_{gb} + Q_{gc} + Q_{gd} \quad (26)$$

To mitigate double-frequency oscillations in DC voltage, currents, and reactive and active power at the grid connections, reference currents can be established by removing the oscillatory components of reactive as well as active power. This is accomplished by utilizing the negative as well as positive sequence grid current and voltage components in the $\alpha^{+} - \beta^{+}$ and $\alpha_{-}^{p} - \beta_{-}^{p}$ frames as detailed below.

$$\begin{bmatrix} P_{gset} \\ Q_{gset} \\ P_{gflu} = 0 \\ Q_{gflu} = 0 \end{bmatrix} = \begin{bmatrix} V_{g\beta+} & V_{g\alpha+} & V_{g\beta-}^{p} & V_{g\alpha-}^{p} \\ V_{g\alpha+} & -V_{g\beta+} & V_{g\alpha-}^{p} & -V_{g\beta-}^{p} \\ V_{g\beta-}^{p} & V_{g\alpha-}^{p} & V_{g\beta+} & V_{g\alpha+} \\ V_{g\alpha-}^{p} & -V_{g\beta-}^{p} & V_{g\alpha+} & -V_{g\beta+} \end{bmatrix} \begin{bmatrix} i_{g\beta+} \\ i_{g\alpha+} \\ i_{g\beta-}^{p} \\ i_{g\alpha-}^{p} \end{bmatrix} \quad (27)$$

Consequently, the standard currents for the GSC, both positive and negative sequences, articulated in the positive d-q axis, can be obtained from eq (28) as:

$$\begin{bmatrix} i_{g\beta+} \\ i_{g\alpha+} \\ i_{g\beta-}^{p} \\ i_{g\alpha-}^{p} \end{bmatrix} = \frac{2}{3|D|} \begin{bmatrix} B_{11} & B_{12} \\ B_{21} & B_{22} \\ B_{31} & B_{32} \\ B_{41} & B_{42} \end{bmatrix} \begin{bmatrix} P_{gset} \\ Q_{gset} \end{bmatrix} \quad (28)$$

The compensatory (negative sequence) term is eventually integrated into the required currents to provide a stable DC connection voltage and uphold "Unity Power Factor (UPF)". This yields the d-q axis reference currents for the GSC, which may be articulated as:

$$i_{g\alpha(ref)} = i_{g\alpha+(ref)} + i_{g\alpha-(ref)}^{p} \quad (29)$$

$$i_{g\beta(ref)} = i_{g\beta+(ref)} + i_{g\beta-(ref)}^{p} \quad (30)$$

$$\text{Where } |D| = (V_{g\beta+}^2 + V_{g\alpha+}^2)^2 - (V_{g\beta-}^{p2} + V_{g\alpha-}^{p2})^2$$

$$\begin{aligned} B_{11} &= V_{g\beta+}^3 + V_{g\beta+}V_{g\beta-}^{p2} + V_{g\beta+}V_{g\alpha-}^{p2}, & B_{31} &= -V_{g\beta-}^3 + V_{g\beta+}^2 V_{g\beta-}^{p} + V_{g\beta-}^{p} V_{g\alpha-}^{p2} \\ B_{12} &= V_{g\alpha+}^3 - V_{g\alpha+}V_{g\beta-}^{p2} - V_{g\alpha+}V_{g\beta-}^{p2} & B_{32} &= -V_{g\alpha-}^{p3} + V_{g\alpha+}^2 V_{g\alpha-}^{p} - V_{g\alpha-}^{p} V_{g\beta-}^{p2}, \\ B_{21} &= V_{g\alpha+}V_{g\beta+}^2 + V_{g\alpha+}V_{g\beta-}^{p2} + V_{g\alpha+}V_{g\alpha-}^{p2} & B_{41} &= -V_{g\alpha-}^{p3} - V_{g\alpha-}^{p} V_{g\beta-}^{p2} + V_{g\alpha-}^{p} V_{g\beta-}^{p2}, \\ B_{22} &= -V_{g\beta+}V_{g\alpha+}^2 + V_{g\beta+}V_{g\beta-}^{p2} + V_{g\beta+}V_{g\alpha-}^{p2}, & B_{42} &= V_{g\beta-}^{p3} + V_{g\beta-}^{p} V_{g\alpha-}^{p2} - V_{g\beta-}^{p} V_{g\alpha+}^2. \end{aligned} \quad (31)$$

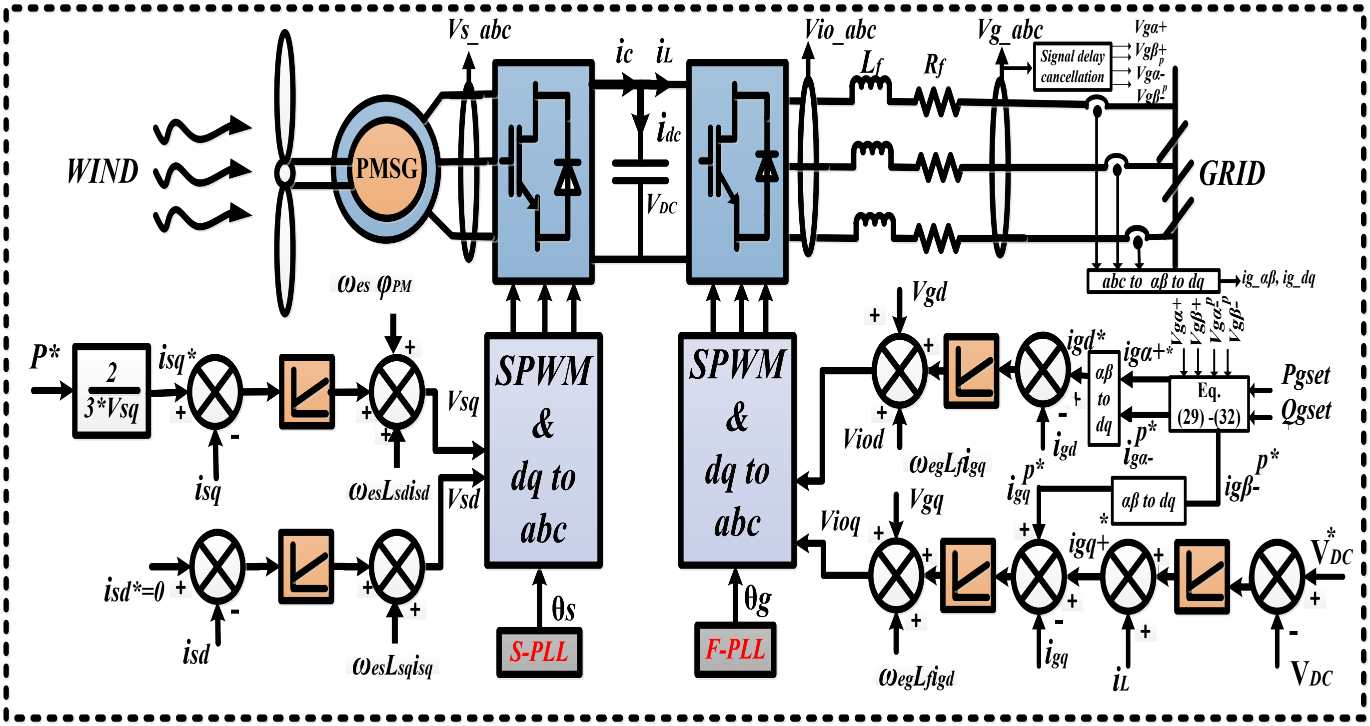

Fig. 2: Schematic representation of the PMSG system incorporating the suggested methodology.

MSC Control of PMSG Using Computed Rotor Speed

Precise speed data is crucial for effective power regulation in imbalanced grid settings. The suggested speed calculation method determines speed utilizing stator d-q electrical voltages and current. Despite grid voltage imbalance, a rotor flux-based S-PLL demonstrates efficacy in determining the orientation θs of the voltage across the stator vector. The position can be promptly approximated by employing the calculated angular frequency with the rotor's enduring electromagnet flux (fixed at 0.26) as the standard input for the phase detectors.

The following is the process for determining the angle of rotation of the stator flux $\omega_{es(cal)}$ using the predicted location of the voltage across the stator vector θs derived from S-PLL:

$$\omega_{es\,(cal)} = \frac{V_{sq} - R_s i_{sq} - \frac{d\varphi_{sq}}{dt}}{\varphi_{sd}} = \frac{V_{sq} - R_s i_{sq} - \frac{d\varphi_{sq}}{dt}}{L_{sd} i_{sd} + \varphi_{PM}} \quad (32)$$

Careful consideration of the initial-order filtering function of transfer must go into the layout of the PI controller's characteristics in order to reduce S-PLL response latencies. An examination of the sensitivity of both R_s and L_s regarding the speed calculation approach, as outlined in Section V, has demonstrated their influence to be minimal. By doing away with the requirement for dual or double vector control, this work offers an improved control method that reduces the total amount of controllers for PI to 3. Moreover Under the assumption of a balanced current distribution in the PMSG system, the stator voltage V_s in the d-q referenced frames can be written as:

$$V_{sd} = R_s i_{sd} - L_{sd}\frac{di_{sd}}{dt} - \omega_{es(cal)} L_{sq} i_{sq} \quad (33)$$

$$V_{sq} = R_s i_{sq} - L_{sq}\frac{di_{sq}}{dt} + \omega_{es(cal)}(L_{sd} i_{sd} + \varphi_{PM}) \quad (34)$$

Equilibrium correction of the cross-coupling factors in eq (33) and (34) is required to get the d-q axis controlling voltage for MSC current management can be observed from fig. 3.

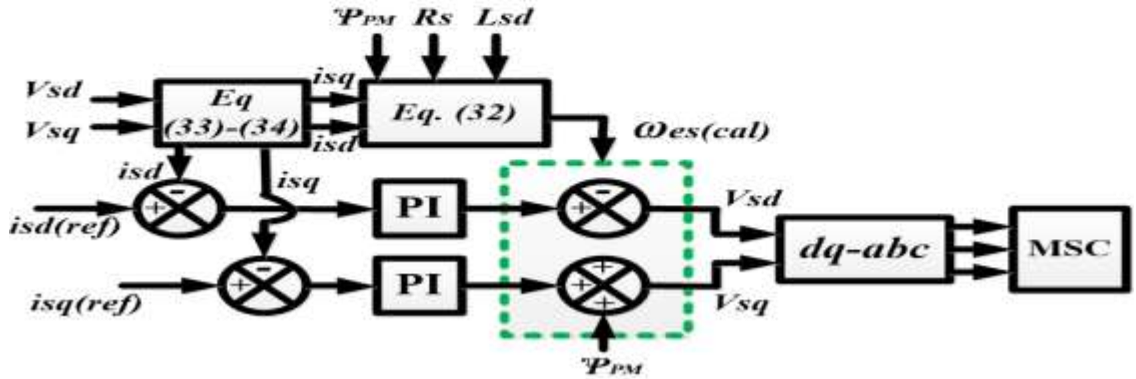

Fig. 3: Schematic Diagram of MSC control

Performance Analysis of Computed Angular speed under PMSG Parameter Variations

The effectiveness of the proposed approach for speed computation, which determines rotor speed using the computed angular stator flux frequency, depends on machine parameters. Therefore, a system analysis is conducted to evaluate the impact of these parameters on the computed speed, as outlined below:

A. Sensitivity Analysis of Stator Flux Frequency (Angular Speed Computation Method)

The reliability of the Angular Speed Calculation Technique is evaluated in relation to uncertainties in machine variables, as the calculation of angular stator flux rate depends on these factors. Mutual inductance may vary due to alterations in the magnetic permeation of both rotor and stator cores under diverse operating conditions, whereas winding resistance may change due to temperature fluctuations. A sensitivity analysis is conducted to evaluate the impact of deviations in key machine parameters, including stator resistance, self-inductance, and rotor flux, from their rated values. Each parameter is examined individually, and the sensitivity function of any variable is determined by differentiating the function with respect to the corresponding parameter. The sensitivity of ω_{es} to variations in different machine parameters is calculated as follows:

$$\mathcal{S}_{\omega_{es}}^{R_s} = -\frac{R_{sN}}{\varphi_{s\beta+}}\frac{i_{s\alpha+}}{\omega_{es}};\ \mathcal{S}_{\omega_{es}}^{L_s} = -\frac{L_{sN}}{\varphi_{s\beta+}}\frac{i_{s\alpha+}}{\omega_{es}} \tag{35}$$

$$\mathcal{S}_{\omega_{es}}^{\varphi_{PM}} = -\frac{\varphi_{PMN}}{\varphi_{s\beta+}} \tag{36}$$

where, R_{sN}, L_{sN} and φ_{PMN} are The nominal quantities for system variables are provided in the Appendix. the Appendix. Further, the sensitivity analysis of the angular speed computation scheme is carried out using (35) and (36) by varying the machine parameters (considering one at a time) from -10% to +10% of their nominal values. It is observed that the computation method is slightly sensitive to the variations in R_s, L_s and φ_{PM}. Given that the leakage flux channel is airborne, fluctuations in stator leakage inductance are irrelevant. Moreover, it is evident from Fig. 4 that the responsiveness of the speed computing approach is significantly diminished due to fluctuations in stator impedance and rotor flow. Consequently, it confirms the effectiveness of the proposed strategy regarding its sensitivity to variations in machine parameters.

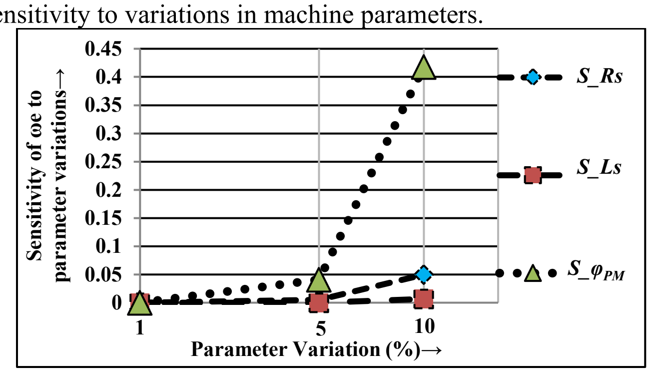

Fig. 4. Sensitivity analysis of angular speed computation method.

B. Stability Analysis of Small signal model for S-PLL.

The proposed feed forward Stator PLL (S-PLL) method for rotor position and angular frequency computation of PMSG in stable and unstable grid condition is proposed in this section. For the grid synchronization the improved S-PLL is similar to F-PLL. The voltage at d-axis (V_{sd+}) is taken as reference for the grid side PLL similarly the permanent magnet (Ψ_{PM}=0.26) is used to designed S-PLL. Here, for the locking the rotor position taken the reference value S-PLL is designed.

Hereafter, the permanent magnet (Ψ_{PM}=0.26) is compare with $\Psi_{PM(actual)}$ (10) and the error generated from the phase detector is provided as input to the PI controller. The output of the PI controller ($\Delta\omega_r$) is added to feed forward signal (ω_r) and the rotor position will be obtained from time integral of (ω_r+ $\Delta\omega_r$).

Since $\Psi_{PM(actual)}$ is obtained from (10) using low pass filter (LPF) then time delay will be occur in S-PLL. However, PI controller parameters has to be selected suitably to compensate the delay taking into account of the filter transfer function as mentioned,

$$\text{LPF}_1 = \text{FPF}_2 = \frac{\omega_C}{S+\omega_C} \quad (37)$$

So the small signal model open loop transfer function can be generated of S-PLL as figure 5.

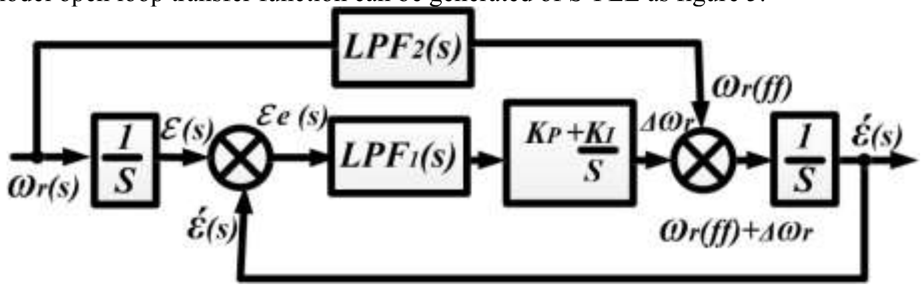

Fig. 5: Small Signal Model of the mentioned S-PLL

$$G_{OL}(S) = \frac{S^2\omega_C + K_P S\omega_C + K_i\omega_C}{S^3} \quad (38)$$

Hereafter the closed loop transfer function can be obtained as

$$\frac{\varepsilon'}{\varepsilon} = \frac{S^2\omega_C + (K_P S + K_i)\omega_C}{S^3 + S^2\omega_C + (K_P S + K_i)\omega_C} \quad (39)$$

Moreover, The stability requirements can be obtained by applying the Routh–Hurwitz stability criterion to the characteristic equation of the RPLL given in equation (36). This procedure leads to the necessary and sufficient conditions for the system stability as,

$$\omega_C > 0;\ K_P\omega_C > K_i;\ \text{and}\ \ K_i\omega_C > 0 \quad (40)$$

Where ω_C represents the filter cut-off frequency. For the better system stability the K_P and K_i can be designed using (40)
It can further be demonstrated that, even when the speed changes linearly, the proposed S-PLL maintains an almost zero steady-state error.

Simulation Results and Discussion

This section showcases the outcomes of a 2.5kW PMSG control performance assessment conducted using PSCAD/EMTDC. Detailed in the appendices are the system characteristics. The investigation takes into account five distinct instances of grid imbalance, which encompass voltage faults: At time t=5s, a single aspect of the grid experiences a voltage dip of fourteen percent in Case I. At t=5s, there is a concurrent drop of 14% in stage B and 12% in stage A voltage in Case II. In Case III, too, at t=5s, the voltage drops in all three phases—10% in stage A, 12% in stage B, and 18% in stage C. Case IV involves a malfunction in stage A at time t=5s that affects the PMSG. Similarly, at t=5s in Case V, a single stage voltage dip of 80% is introduced. Pgset= 1.85 kW, Qgset= 0 kVar, and Vdc(ref)= 460V are the default values used in this inquiry. Grid currents, reactive power, active power, and DCLV will all fluctuate when the grid voltage is not balanced.
Both Figure 6(a) and Figure 6(d) display the results of the simulation for the stator's calculated angular velocity and position. Even with grid imperfections present, these findings show that the suggested approach can reliably estimate location and speed. Regardless of grid disruptions, this renders it a reliable method for PMSG generation and control.
When the system experiences voltage imbalance, the PMSG parameters are affected by double-frequency components, resulting in harmonics in the grid currents. Case I analyzes the effect of a 14% voltage dip occurring in a single phase of the grid while maintaining a constant speed at t=5 sec Consequently, essential system variables— certain variables—including active and reactive power within the grid, currents flowing through the grid, and DCLV—begin to oscillate at a rate that is double that of the grid (100 Hz). Under unbalanced grid voltage conditions, the MSC continues to extract power from the generator. This excess energy accumulates at the DC-link capacitor, leading to an increase in DC-link voltage. Consequently, the GSC is subjected to overvoltage stress, which may force it to operate beyond its current handling limits.

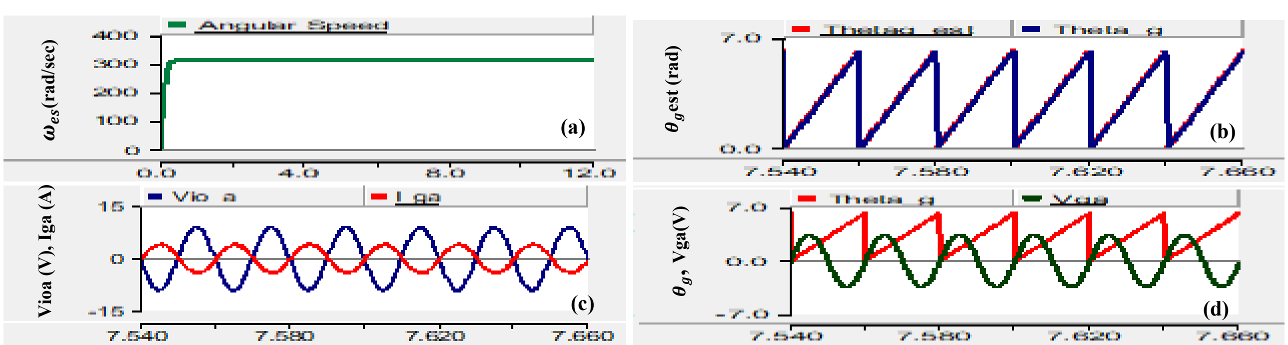

Fig. 6: Simulation results: (a) Angular speed (rad/sec), (b) Actual and calculated position (elec rad), (c) Scaled A-stage GSC voltage (V) and grid current(A) and (d) Position (elec rad) and Scaled A-phase grid voltage (V).

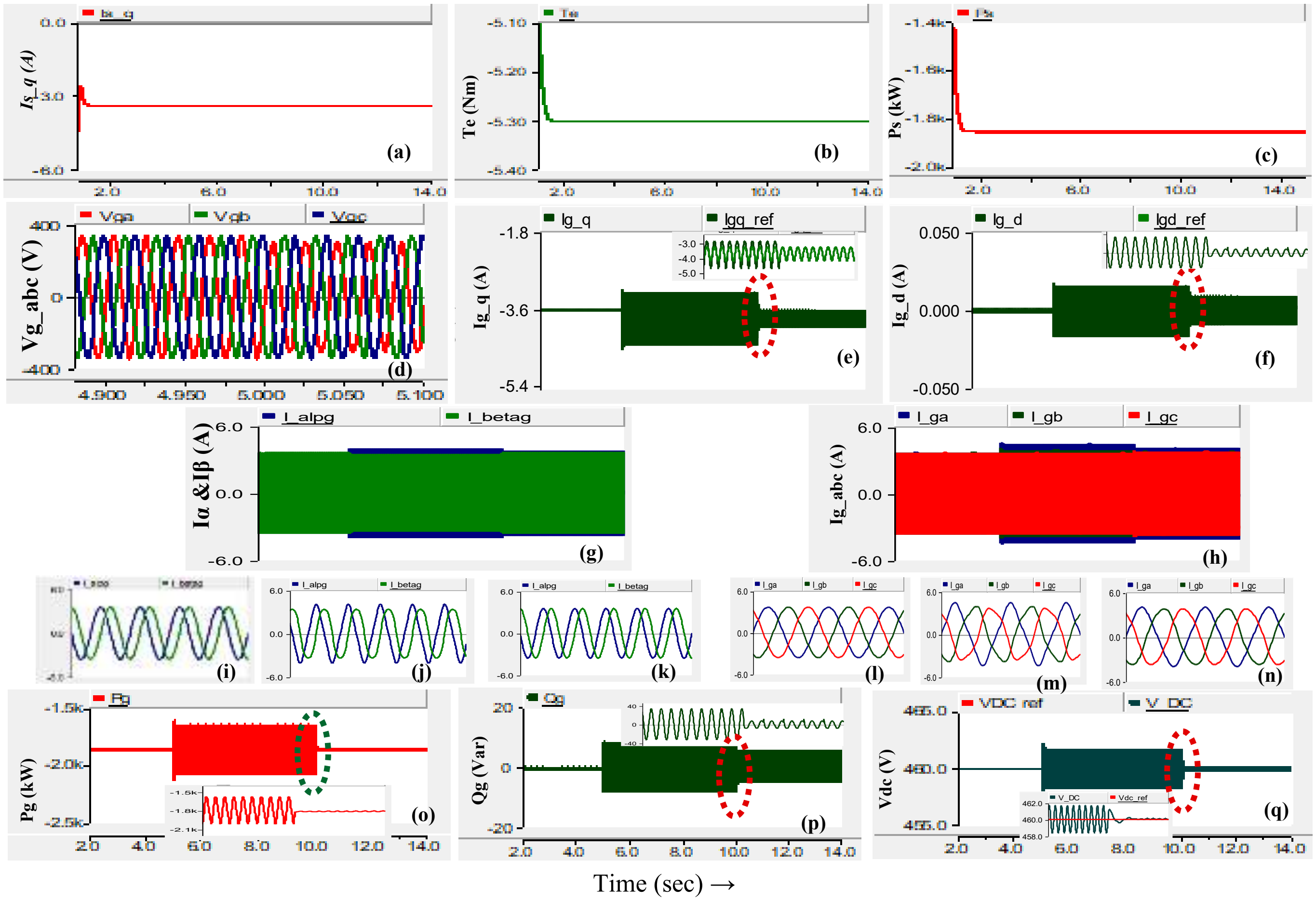

Fig. 7: Simulation outcomes indicating a 14% reduction in phase "A": (a) q-axis current at machine side (A), (b) Electromagnetic Torque (N-m), (c) Active power at stator side (d) Grid Voltages (V), (e) q-axis current at grid side (A), (f) d-axis current at grid side (A), (g) α-β axes grid currents (A), (h) GSC currents (A), (i) Zoomed view of balanced α-β axes grid currents (A), (j) Zoomed view of distorted currents α-β axes grid currents (A), (k) Zoomed view of controlled α-β axes grid currents (A), (l) Zoomed view of balanced grid currents (A), (m) Zoomed view of distorted Grid Currents (A), (n) Zoomed view of controlled grid Currents (A), (o) Active power at grid side; (p) Grid side Reactive Power (Var) and (q) DC link voltage.

Case I: In this scenario, a 14% voltage dip is introduced in one phase of the grid while maintaining a constant speed at t= 5sec. At twice the grid rate (100 Hz), important system variables such grid currents, both reactive and active power on the grid, and DCLV start to oscillate. Figure 7 shows that 12.05.0% of grid-side power that is active, 4.22% of reactive power, 13.07% of grid current, and 0.422 % of the DCLV are oscillating. The "total harmonic distortion (THD)" resulting from this 14% dip is measured at 7.40%.

However, when the controller is activated at t= 10 sec, these oscillations are significantly reduced to 0.497%, 1.73%, 7.37%, and 0.0152%, respectively. Notably, the grid currents maintain a sinusoidal waveform with a low THD of 2.97%, despite being unbalanced.

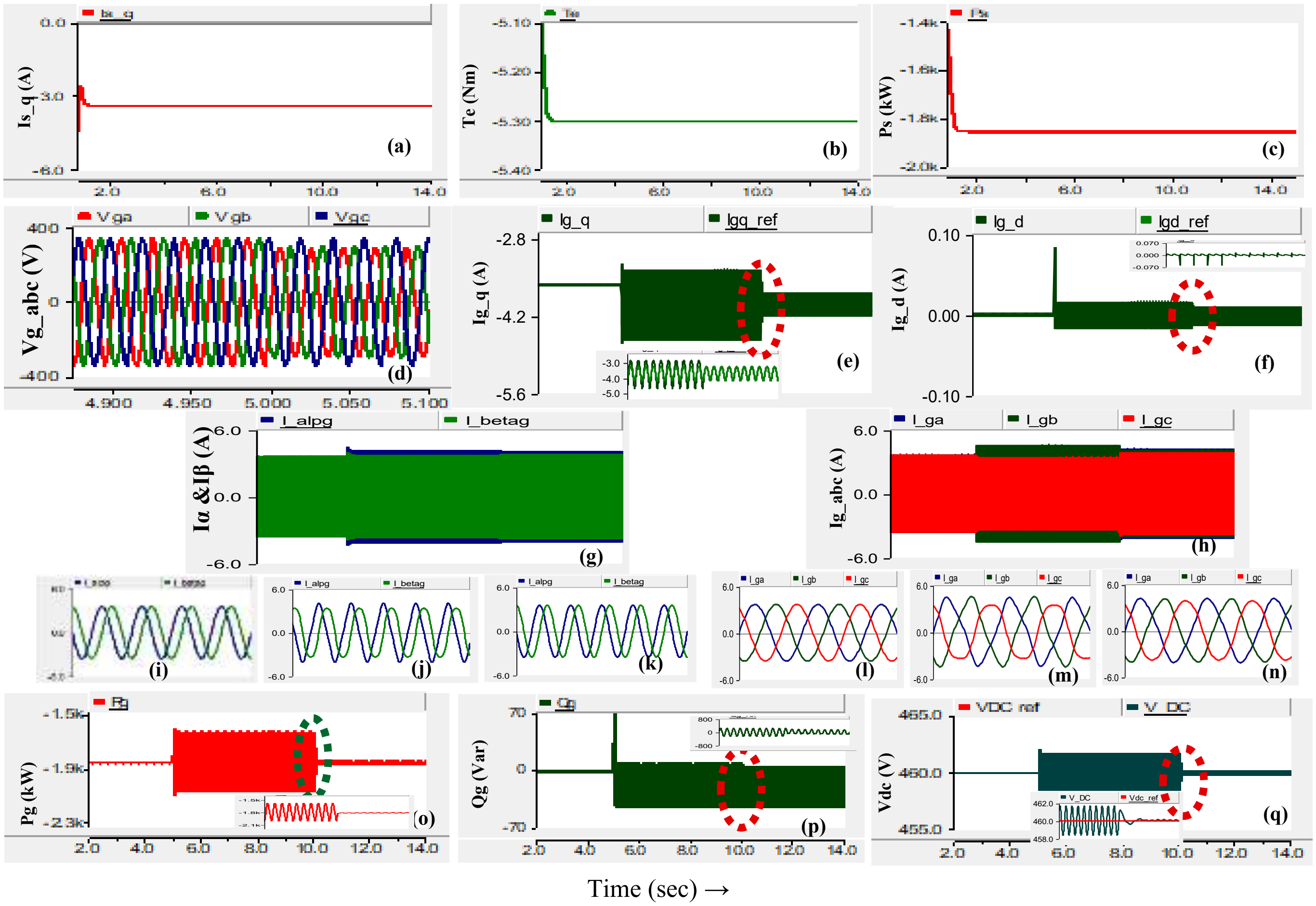

Fig. 8: Findings with 14% dip in phase "A" and 12% dip in Phase "B": (a) q-axis current at machine side (A), (b) Electromagnetic Torque (N-m), (c) Active power at stator side (d) Grid Voltages (V), (e) q-axis current at grid side (A), (f) d-axis current at grid side (A), (g) α-β axes grid currents (A), (h) GSC currents (A), (i) Zoomed view of balanced α-β axes grid currents (A), (j) Zoomed view of distorted currents α-β axes grid currents (A), (k) Zoomed view of controlled α-β axes grid currents (A), (l) Zoomed view of balanced grid currents (A), (m) Zoomed view of distorted Grid Currents (A), (n) Zoomed view of controlled grid Currents (A), (o) Active power at grid side; (p) Grid side Reactive Power (Var) and (q) DC link voltage.

Case II: Here, at t=5s, the PMSG is running at a constant rate of 314 rad/sec and concurrently encounters a voltage dip of 12% in stage A and 14% in stage B of the grid. Figure 8 shows that active power on the grid, current, reactive electricity, and DC link voltage all show oscillations of 18%, 23%, 52%, and 0.65%, correspondingly. The THD in the grid current due to this energy dip is measured at 5.44%. However, when the controller is activated at t=10s, these oscillations are significantly reduced to 7.7e-3%, 0.1%, $7.8e^{-3}$% and $4.2e^{-4}$% respectively. Notably, the grid currents maintain a sinusoidal waveform with a low THD of 3.11%, despite being unbalanced.

Case III: In this scenario, the PMSG undergoes a simultaneous voltage dip across all three phases—10% in stage A, 12% in B, and 14% in C time t=5s while maintaining a continuous speed of 314 rad/sec. As shown in Fig. 8, the resulting oscillations in grid-side active power, reactive power, grid current, and DC link voltage are 1.6%, 21%, 1.64%, and 0.05%, respectively. Without the controller, The total harmonic distortion in the grid current resulting from the voltage drop is 7%. However, upon activating the controller at t=10s, these oscillations are significantly reduced to $13e^{-3}$%, 0.1%, $5.4e^{-3}$% and $3.6e^{-4}$% respectively. Notably, despite being unbalanced, the grid currents maintain a sinusoidal waveform with a low THD of 3.86%. Additionally, as illustrated in Fig. 9, the THD in grid currents remains below 5% across all tested cases.

Case IV: In this scenario, the PMSG experiences a fault in phase A at time t=5s all the while maintaining a steady velocity of 314 rad/sec. As shown in Fig. 10, the resulting shifts in active power on the grid, reactive power, grid current, and DCLV are 86.56%, 72%, 87.23%, and 9.28%, respectively. Without the controller, the THD in the grid current due to the fault in phase A is 11.23%. However, after activating the controller at t=10s, these oscillations are significantly reduced to 12.32%, 17.36%, 32.23%, and 2.16%, respectively. Notably, despite being unbalanced, the grid currents maintain a sinusoidal waveform with a lower THD of 5.2%.

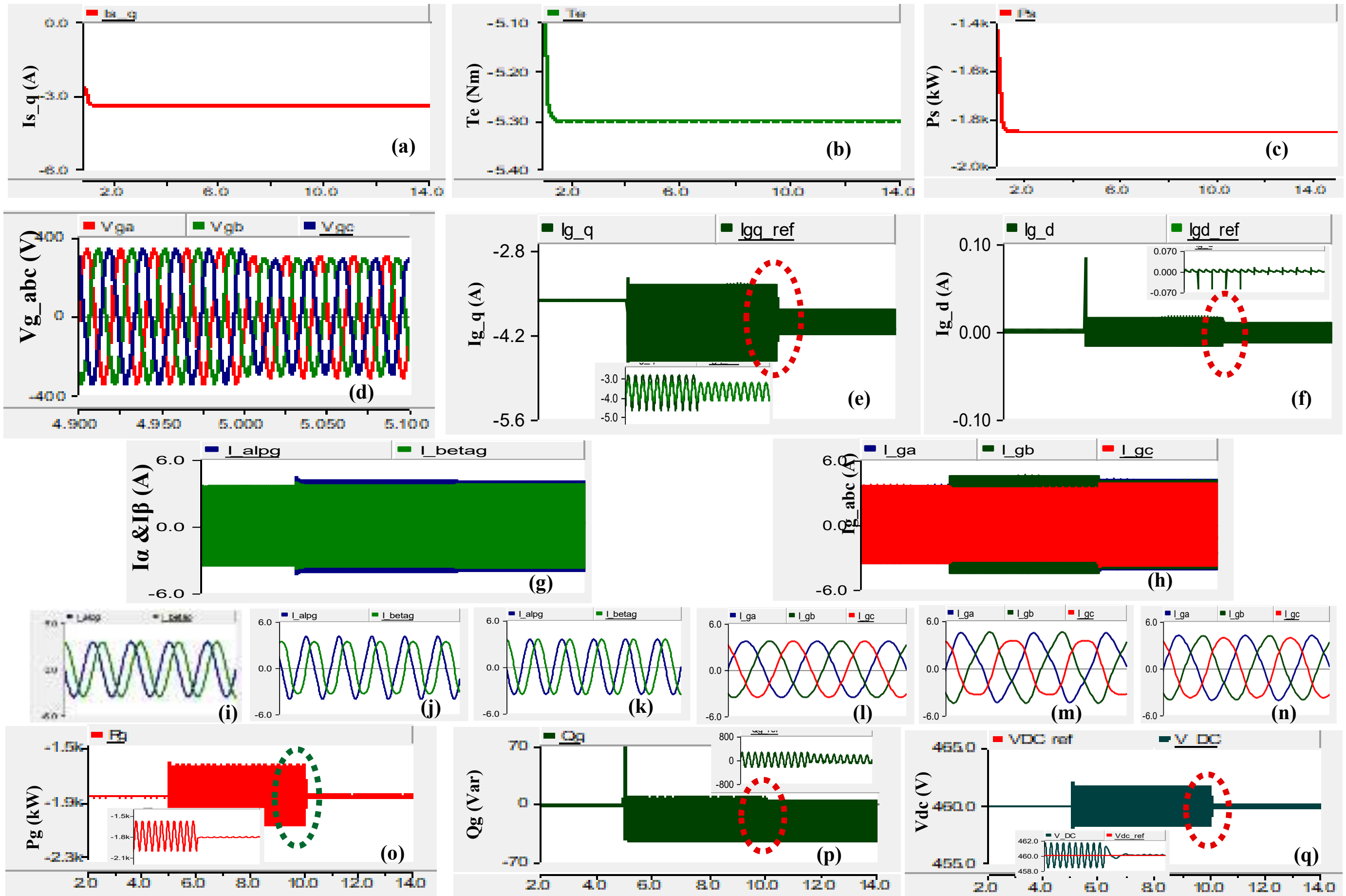

Time (sec) →

Fig. 9: with 10% dip in phase "A" & 12% dip in Phase "B" and 14% dip in Phase "C": (a) q-axis current at machine side (A), (b) Electromagnetic Torque (N-m), (c) Active power at stator side (d) Grid Voltages (V), (e) q-axis current at grid side (A), (f) d-axis current at grid side (A), (g) α-β axes grid currents (A), (h) GSC currents (A), (i) Zoomed view of balanced α-β axes grid currents (A), (j) Zoomed view of distorted currents α-β axes grid currents (A), (k) Zoomed view of controlled α-β axes grid currents (A), (l) Zoomed view of balanced grid currents (A), (m) Zoomed view of distorted Grid Currents (A), (n) Zoomed view of controlled grid Currents (A), (o) Active power at grid side; (p) Grid side Reactive Power (Var) and (q) DC link voltage.

Case V: Under the considered operating condition, the PMSG system runs at a constant rotor speed of 314 rad/s while experiencing an 80% voltage sag in phase A at t=5s. The system response exhibits a behavior comparable to previously analyzed cases, as illustrated in Figure 11. After the proposed controller is enabled, noticeable suppression of oscillations is observed in grid-side active power, reactive power, grid current, and DC-link voltage. The control approach effectively maintains system stability even during severe grid unbalance and fault conditions. Furthermore, a comparative evaluation is carried out based on the percentage reduction of oscillations in Pg, Qg and Vdc. The simulation outcomes verify that the proposed reference current generation approach achieves better oscillation suppression and dynamic stability than existing methods reported in the literature. The controller effectively minimizes fluctuations in active power, reactive power, and DC-link voltage during fault and unbalanced grid conditions. As a result, the proposed strategy enhances the low-voltage ride-through capability and ensures reliable operation of grid-connected PMSG-based wind energy conversion systems under disturbed grid conditions.

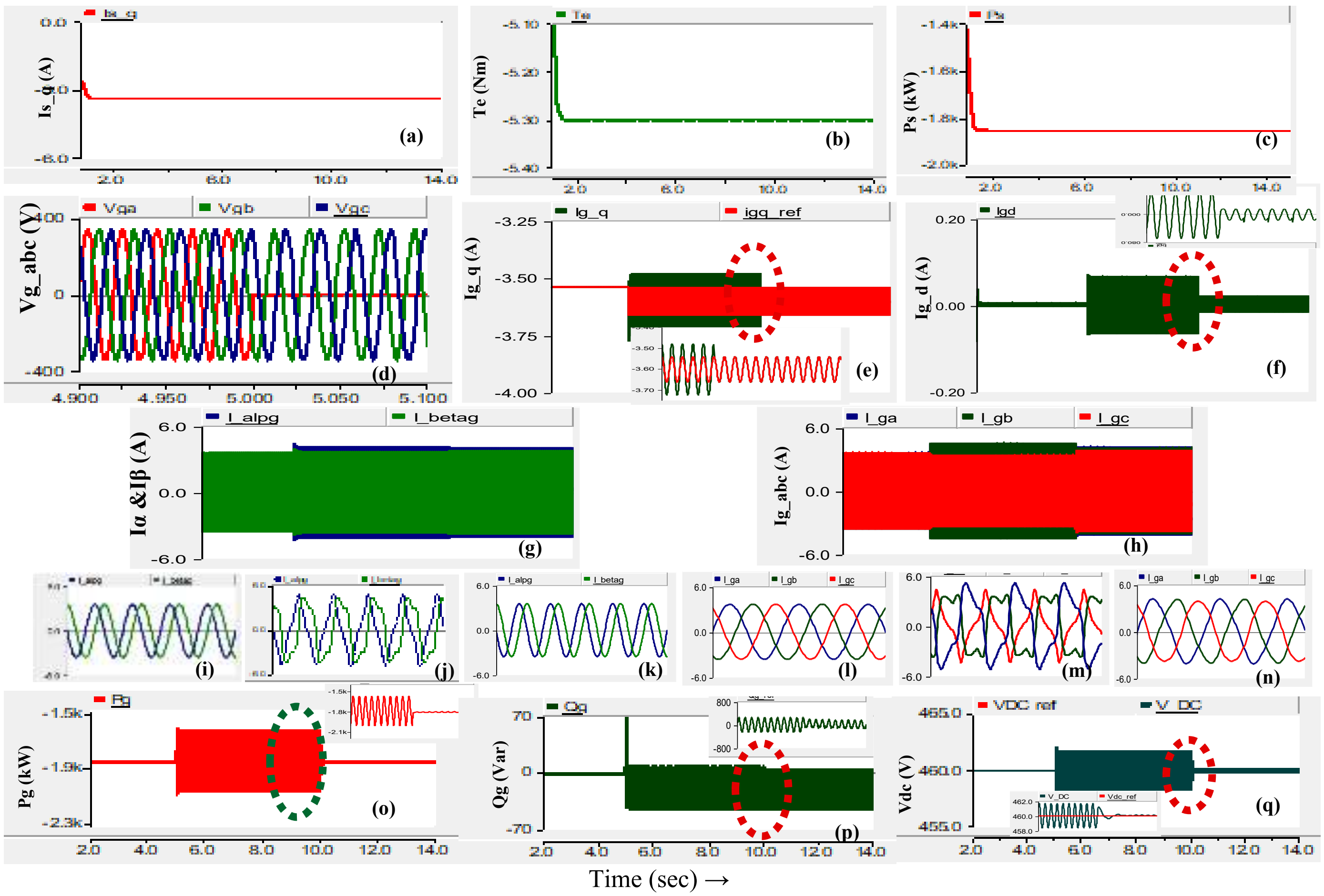

Fig. 10: Simulation results with fault in phase "A": (a) q-axis current at machine side (A), (b) Electromagnetic Torque (N-m), (c) Active power at stator side (d) Grid Voltages (V), (e) q-axis current at grid side (A), (f) d-axis current at grid side (A), (g) α-β axes grid currents (A), (h) GSC currents (A), (i) Zoomed view of balanced α-β axes grid currents (A), (j) Zoomed view of distorted currents α-β axes grid currents (A), (k) Zoomed view of controlled α-β axes grid currents (A), (l) Zoomed view of balanced grid currents (A), (m) Zoomed view of distorted Grid Currents (A), (n) Zoomed view of controlled grid Currents (A), (o) Active power at grid side; (p) Grid side Reactive Power (Var) and (q) DC link voltage.

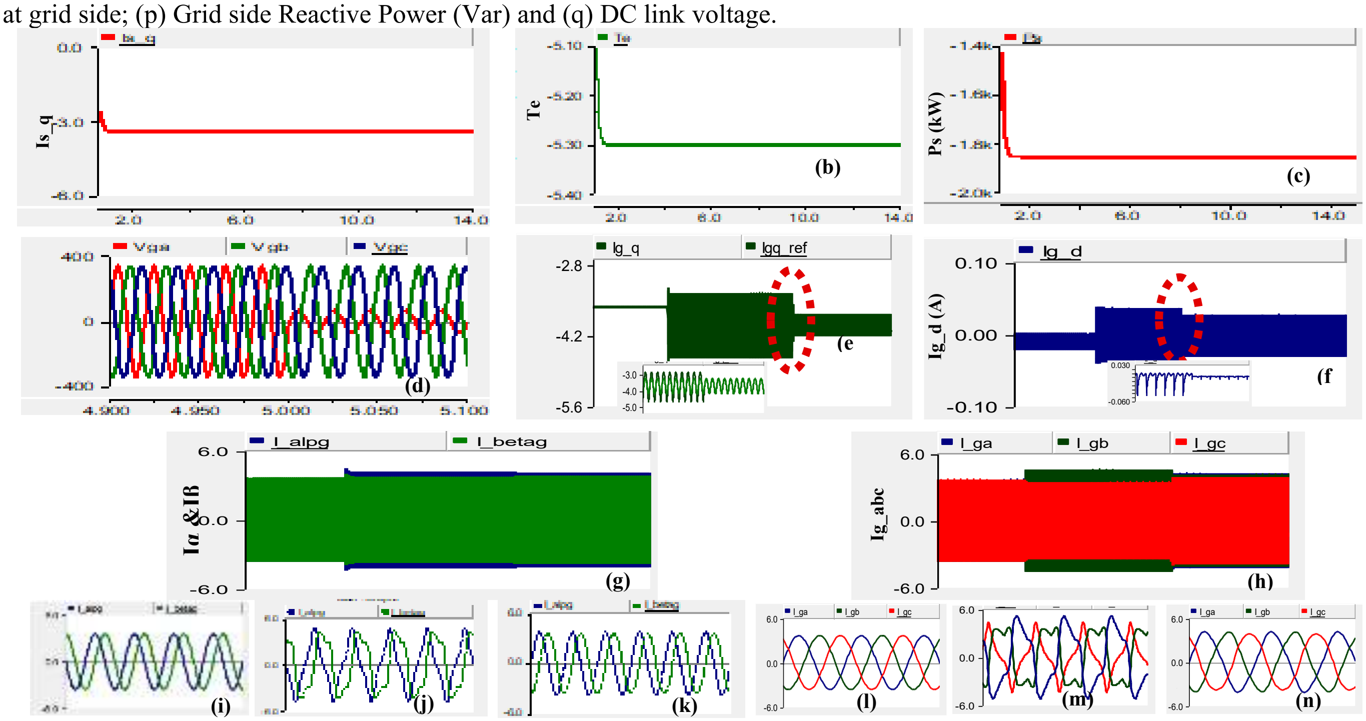

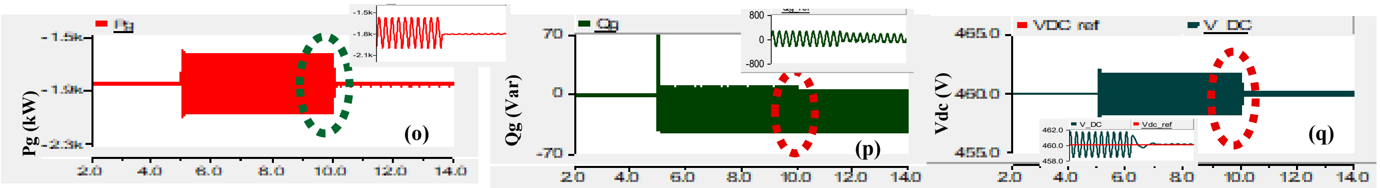

Time (sec) →

Fig. 11: Simulation 80% dip in stage "A" : (a) Grid Voltages (V), (b) q-axis current at grid side (A), (c) d-axis current at grid side (A), (d) α-β axes grid currents (A), (e) Zoomed view of balanced α-β axes grid currents (A), (f) Zoomed view of distorted currents α-β axes grid currents (A), (g) Zoomed view of controlled α-β axes grid currents (A), (h) GSC currents (A), (i) Zoomed view of balanced grid currents (A), (j) Zoomed view of distorted Grid Currents (A), (k) Zoomed view of controlled grid Currents (A), (l) Active power at stator side and grid sid; (m) grid side Reactive Power (Var) and (n) DC link voltage.

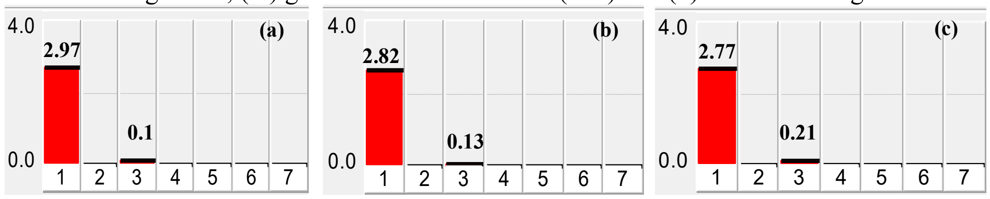

Fig. 12: Simulation results of grid current THD under different cases of voltage dip: (a) THD under 14% single line voltage dip; (b) THD under 12% & 14% voltage dip in double line and (c) THD under 10%, 12% and 14%voltage dip in triple line.

Real Time Simulation in OPAL-RT OP4510

By utilizing the OPAL-RT OP4510 real-time electrical grid digital simulators, as illustrated in the test configuration in Fig. 13, we can confirm that the suggested strategy effectively reduces pulses in grid-side electrical power, DCLV and reactive power while guaranteeing sinusoidal network-side currents. To further examine the outcomes of the OPAL-RT hardware, two case investigations have been carried out. Case I involved analyzing the PMSG with OPAL-RT after a 7% voltage fall in phase A at t=4s. Figure 14 shows that the active power on the grid current as well and DC link grid and reactive power value all experienced fluctuations of 13%, 32%, 0.85% and 8%, correspondingly. Grid currents had a THD of 5.44 percent. Nevertheless, these oscillations were considerably diminished to 6.6e-3%, 0.21%, 5.2e −3%, and 0.13e −4% respectively after the controller was activated at t=6s. Even though they are imbalanced, the grid currents maintain a low THD of 3.56% and continue to be sinusoidal. Case II used OPAL-RT for analysis after subjecting the PMSG to a 9% voltage dip in stage A at t=4s. Figure 15 shows that between 10% and 15% of grid-side active power, 36% of grid current, and 0.935% of DC link voltage oscillated. The THD in grid currents was measured at 6.24%. Nonetheless, subsequent to the activation of the controller at t=6s, the fluctuations in grid-side active electricity, reactive power, grid current, and DCLV were markedly diminished to $7.3e^{-3\%}$, 0.41%, $7.3e^{-3\%}$, and $0.27e^{-4\%}$ respectively. Importantly, the grid currents keep a sinusoidal waveform with a reduced THD of 3.86% even if they are imbalanced. In addition, Table I shows the comparative analysis of PMSG Performance with different control schemes under unbalanced grid voltages for evaluating the PMSG system's efficiency.

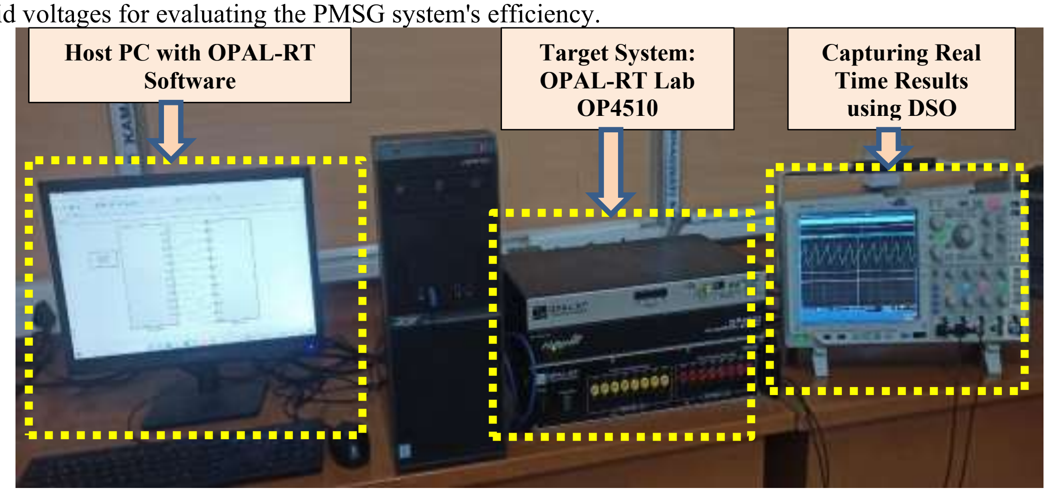

Fig. 13: OPAL-RT Hardware-in-the-Loop Test Configuration.

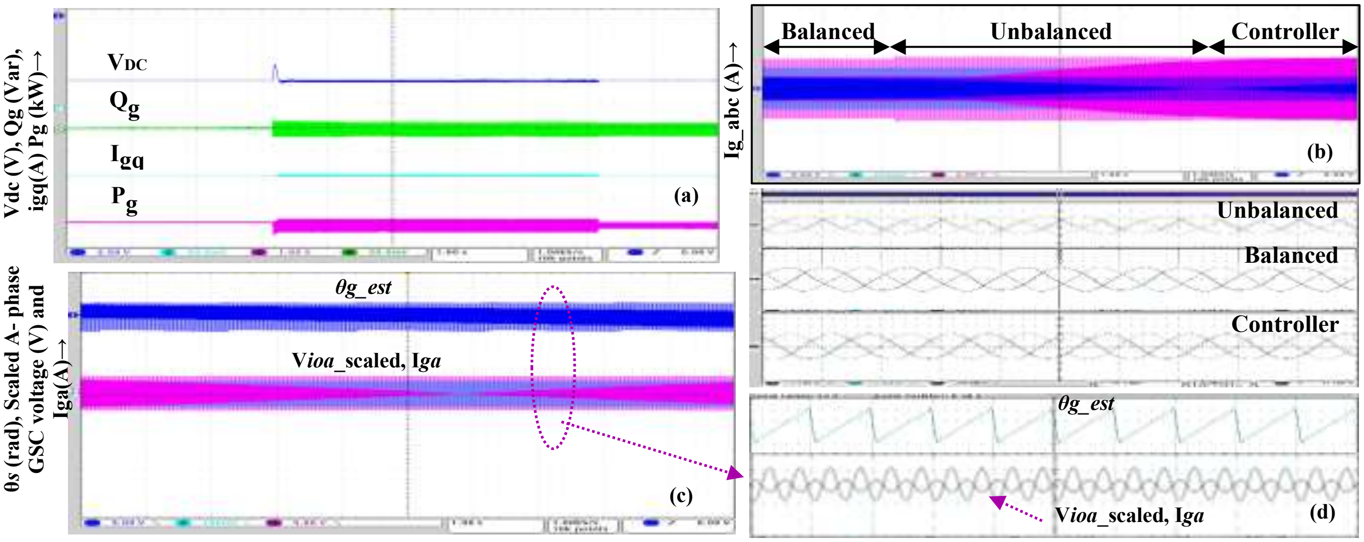

Fig. 14: OPAL-RT findings indicate a 7% decrease in phase "A" at the grid interface: DC link voltage (Vdc) (V), Reactive power (Qg) (Var), Grid current on the q-axis (igq) (A), Active power (Pg) (kW), (b) Grid currents (ig_abc) (A), (c) Position θs_est (elec. rad) and Scaled A- phase GSC voltage (V) and (d) zoomed view of balanced, unbalanced and controller of grid current, Position and Scaled A- phase GSC voltage (V) and grid current (A).

Additionally, the grid side converter has been tasted at different grid voltage unbalanced conditions and it is found that beyond 35 % dip in grid voltage the converter will not be able to provide compensation current because is reaches its rated current and voltage limit as shown in fig. 16. The analysis shows that the grid side active power pulsations exceed the rated value with 40% oscillations (Fig. 16a) in grid voltage without the proposed controller, while dc link voltage exceeds the rated value with 25% oscillations (Fig. 16b) and 34% oscillations in grid side current (Fig. 16c) respectively. Similarly in fig. 12 it is noticed that THD under 14% dip in single line is 2.97 (fig. 12a) while THD under 12% & 14% voltage dip in double line is 2.82 (fig. 12b) and THD under 10%, 12% and 14% voltage dip in triple line is 2.77 (Fig. 12c) respectively.

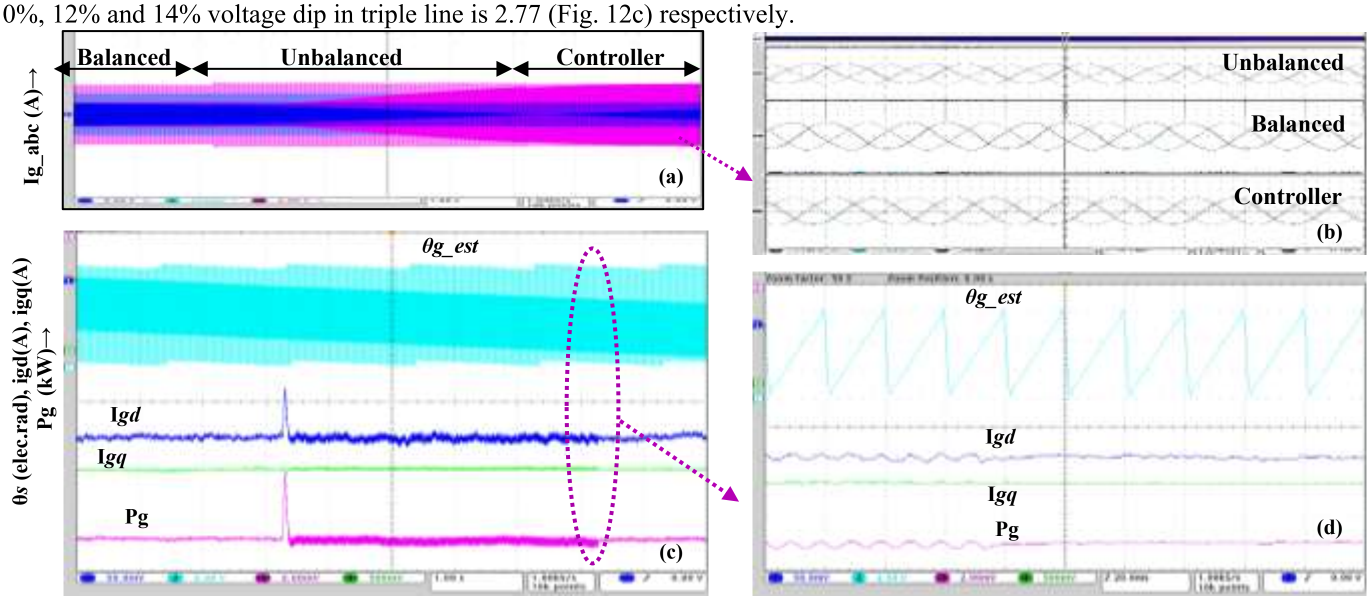

Fig. 15: OPAL-RT results with 9% dip in phase “A” at grid side: (a) Grid currents (ig_abc) (A), (b) zoomed view of balanced, unbalanced and controller of grid current (c) Position θs_est (elec. rad), grid current at d-axis (igd), grid current at q-axis (igq) and Active power (Pg) (kW) and (d) zoomed view off Position θs_est (elec. rad), grid current at d-axis (igd), grid current at d-axis (igd) and Active power (Pg) (kW).

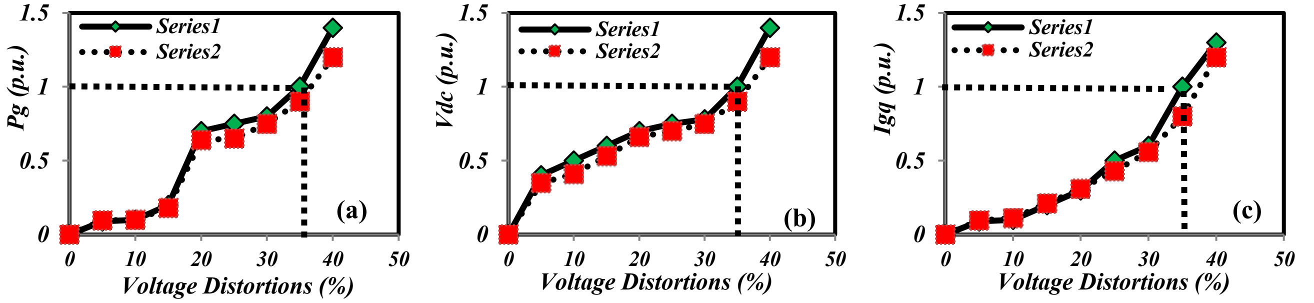

Fig. 16: Converters performance under voltage dips: (a) Grid side active power (Pg) (p.u.), (b) DC link Voltage (p.u.) and (c) Grid side current at q-axis (p.u.). [Series1→Without Conrtoller and Series2→With Controller.]

Conclusion

A novel advanced current re generation scheme for the GSC is proposed in the study for grid connected PMSGs based on rotor in the positive stationary α–β reference frame, flux-oriented vector control. The proposed scheme use only the positive sequence components of stator current and voltage for estimating the reference current with no Phase-Locked Loop (PLL) used. An improved stator flux calculation method is utilized to calculate rotor position and angular velocity based on the calculated stator flux frequency. This approach efficiently handles unbalanced grid voltages, which normally cause 100 Hz vibrations in output power, grid currents, and DCLV due to the presence of negative sequence components. The resultant control scheme effectively eliminates such oscillations by removing harmonic power terms at double the grid angle, thus enhancing the dynamic performance. It keeps stator and grid current sinusoidal waveforms and has a unity power factor at the grid side even in grid fault conditions. Simulation results reveal dramatic performance gains—for example, in a case where there is a 12% dip in voltage in stage A and a 14% dip in voltage in stage B, the grid current THD decreases from 8.44% to 4.6%, indicating the effectiveness of the method in harmonic reduction. In addition, real-time implementation by the OPAL-RT OP4510 simulator confirms the robustness and practicability in reality of the controller under different distorted grid voltage conditions. The outcomes confirm a significant decrease in power harmonics and oscillations, situating the proposed method as a viable and effective means for improving the stability and power quality of PMSG systems in unbalanced or fault-disturbed grid conditions.

Table I: Performance Comparison of Different Controllers Employed in Grid-Connected PMSG Systems

Controller	Line	Voltage Fluctuations (%)	P_s	Ψ_{sd}	T_e	THD
Vector Control [5]	Single Line	2	7.20	6.62	0.126	4.30
		5	9.23	11.37	0.34	3.35
		7	11.62	10.48	0.63	4.82
	Triple Line	18 (A-phase)	3.52	4.14	0.03	3.96
		9 (B-phase)				
		13 (C-phase)				
Vector control Integrated DPC [22]	Single Line	2	0.349	2.48	0.012	3.85
		5	0.301	3.78	0.015	3.69
		7	0.379	6.37	0.019	4.02
	Triple Line	18 (A-phase)	$9e^{-3}$	$3.2e^{-3}$	$2.32e^{-4}$	3.63
		9 (B- phase)				
		13 (C-phase)				
Proposed Method	Single Line	2	0.234	2.28	0.01	3.146
		5	0.205	5.78	0.014	3.205
		7	0.297	7.37	0.0182	4.197
	Triple Line	18 (A-phase)	$8.3e^{-3}$	$2.39e^{-3}$	$2.18e^{-4}$	2.754
		9 (B- phase)				
		13 (C-phase)				

Appendix A

Permanent Magnet Synchronous Machine: 2.5kW, 50 Hz, 8-Pole, 415 V, 4.8 A. Machine Parameters: RS=1.28 Ω, Lsd=42.76 mH, Lsq=42.76 mH, J=0.0011$kg-m2$, $\varphi_{PM} = 0.26$ Wb, B=0.001954 kg-m/s2.

Appendix B

PI controller parameters for GSC and MSC control

Controller		K_P	$T_i = \frac{K_P}{K_I}$ (sec)
MSC		**1**	**0.1**
GSC	**Voltage**	**1.68**	**0.1**
	Current	**0.1**	**0.006977**

Nomenclature

φ_{PM}	PMSG rotor flux
P_s, P_g	Machine and Grid side active power
A, B	Stationary frame
D, Q	Synchronously Rotating frame
V, I	Voltage and Current
ω_{es}	Angular rotor speed
Te	Electromagnetic Torque
φ_{sd}, φ_{sq}	Stator flux at d-q frame
Rf, Lf	Filter Resistance and Inductance
C	DC link Capacitor
B	Frictional coefficient
T_L	Load Torque
ω_m	Mechanical speed
J	Moment of Inertia
θ_g, μ	Angle between stator voltage vector and β-axis; stator flux axis and β-axis
MSC	Machine Side Converter
GSC	Grid Side Converter
THD	Total Harmonic Distortion
SL	Single Line
DL	Double Line
TL	Triple Line
DCLV	DC link Voltage

Subscripts

p	Quantity in positive d-q reference frame
io	Inverter output
imb	Imbalance
flu	Fluctuation

Conflict of Interest

The authors declare that they have no known competing financial interest or personal relationships that could have appeared to influence the work reported in this paper.

Data Availability Interest

Data will be provided by the corresponding author upon reasonable request.

Funding Statement

The authors declare that the financial interests/personal relationships which may be considered as potential competing interests.

References

[1] R. Vijayapriya, P. Raja , M.P. Selvan "Enhanced method of rotor speed and position estimation of permanent magnet synchronous Machine based on stator SRF-PLL," Eng. Scie. and Tech. an Inter. Jour., India, pp. 1450-1459, 2017

[2] G. Buticchi, E. Lorenzani, , F. Immovilli, ,and C. Bianchini, "Active Rectifier With Integrated System Control for Microwind Power Systems," IEEE Trans. Sust. Energy, vol. 6, no. 1,pp. 60-69, Jan. 2015.

[3] M. A. Asha Rani, C. Nagamani, , and G. Saravana Ilango, "An Improved Rotor PLL (R-PLL) for Enhanced Operation of Doubly Fed Induction Machine," IEEE Trans. Sust. Energy, vol. 8, no. 1, pp. 117-125, Jan. 2017.

[4] R. Vijayapriya, P. Raja, and M. P. Selvan "A Modified Active Power Control Scheme for Enhanced Operation of PMSG Based WGs, IEEE Trans. Sust. Energy, 2017 IEEE.

[5] M. A. Asha Rani ,C. Nagamani and G.S. Ilango "Compensation of Magnetizing Current for Enhanced Operation of DFIG Under Grid Unbalance," IEEE Trans. Power electon., vol. 32, no. 7, pp. 5214-5225, Jul. 2017.

[6] D. Thakur and J. JIANG “Control of a PMSG Wind-Turbine Under Asymmetrical Voltage Sags Using Sliding Mode Approach,” IEEE Power and Energy Technology Systems Journal, 2018.
[7] M. Rosyadi, A. Umemura, R. Takahashi and J. Tamura “Development of Phasor Type Model of PMSG based Wind Farm for Dynamic Simulation Analysis,” 2016, IEEE.
[8] M. Benadja, M. Rezkallah, S. Benhalima, A. Hamadi and A. Chandra “Hardware Testing of Sliding Mode Controller for Improved Performance of VSC-HVDC Based Offshore Wind Farm Under DC Fault, IEEE Trans. Indus. Appl., vol. 55, no. 2, pp. 2053-2063Mar./Apr. 2019.
[9] B. Prajapati and M. C. Chudasama “Modeling of Grid Connected PMSG based WECS” 2020, IEEE.
[10] M. K. K. Prince, M. T. Arif, A. Gargoom, A. M. T. and Md. E. Haque, “Modeling, Parameter Measurement, and Control of PMSG-based Grid-connected Wind Energy Conversion System,” Journ. Modern sys. Alean Energy, vol. 9, no. 5, pp. 1054-1065, Sept. 2021.
[11] M. E. Zarei, D. Ramírez, M. Prodanovic, G. M. Arana "Model Predictive Control for PMSG-Based Wind Turbines With Over modulation and Adjustable Dynamic Response Time," IEEE Trans on Inds Elecr., vol. 69, no. 2, pp. 1573-1583, Feb. 2022.
[12] H. F. a. X. Zhang, "Improvement of Low-Voltage Ride-Through Capability for Wave Energy Conversion System," IEEE Trans on Inds Elecr., vol. 69, no. 8, pp. 8123-8133, Aug. 2022.
[13] Y. Zhao, Z. Zhang, W. Qiao and L. Wu "An Extended Flux Model-Based Rotor Position Estimator for Sensorless Control of Salient-Pole Permanent-Magnet Synchronous Machines," IEEE Trans on Inds Elecr., vol. 30, pp. 4412-4422, Aug. 2015.
[14] Y. Zhao, Z. Zhang, W. Qiao, L. Wu, "Improved Rotor Position and Speed Estimators for Sensorless Control of Interior Permanent-Magnet Synchronous Machines," IEEE Jour. of Emer. And Selec. Top. in Pow. Elect., vol. 2, no. 3, pp. 627-639, SEPTEMBER 2014.
[15] Y. Hu, Z. Q. Zhu and M. Odavic "Compensation of Unbalanced Impedance of Asymmetric Wind Power PMSG Compensated by External Circuits in Series," CES Trans on Elect Machines and Sys, vol. 1, pp. 180-188, Jun. 2017.
[16] Y. Hu, Z. Q. Zhu, M. Odavic. Lee, Yi Tan and Y. Cao,"An Improved Method of DC Bus Voltage Pulsation Suppression for Asymmetric Wind Power PMSG Systems With a Compensation Unit in Parallel," IEEE Trans. on Ener. Conv., vol. 12, no. 1, pp. 349-359, Jan. 2021.
[17] X. Zeng, J. Yao, Z. Chen, W. Hu, Z. Chen and T. Zhou "Co-Ordinated Control Strategy for Hybrid Wind Farms With PMSG and FSIG Under Unbalanced Grid Voltage Condition," IEEE Trans. On Susta. Energy, vol. 7, pp. 1100-1110, Jul.2016.
[18] Z. Gao, W. Du, T. Zhao, H. Xie, H. F. Wang, and S. Yi, "Transient synchronization stability analysis of a grid-connected wind farm with multiple PMSGs," IEEE Transactions on Power Systems, vol. 39, no. 6, 2024.
[19] T. Dai, X. Xiao, Q. Xie, J. Ren, and Z. Zheng, "Hybrid grid-forming and grid-following PMSG-SMES architecture with enhanced FRT capability," IEEE Transactions on Applied Superconductivity, vol. 34, no. 8, 2024.
[20] R. Basak, G. Bhuvaneswari and R. R. Pillai "Low-Voltage Ride-Through of a Synchronous Generator-Based Variable Speed Grid-Interfaced Wind Energy Conversion System," IEEE Trans on Inds Elecr. APP., vol. 56, no. 1, pp. 752-762, Jan./Feb. 2020.
[21] Y. Zhang and M. Zhan, "Transient synchronous stability analysis of PMSG grid-connected system considering transient switching control under severe faults," IEEE Transactions on Power Electronics, vol. 40, no. 5, 2025.
[22] R. Mishra and T. K. Saha, "Performance Analysis of Model Predictive Technique Based Combined Control for PMSG-Based Distributed Generation Unit," IEEE Trans on Inds Elecr., vol. 67, no. 10, pp. 8991-9000, Oct. 2020.
[23] Y. Ma, J. Xu, C. Gao, G. Li, and K. Wang, "Low-frequency oscillations and resonance analysis of VSG-controlled PMSG-based wind generation systems," Journal of Modern Power Systems and Clean Energy, vol. 13, no. 1, 2025.
[24] M. K. K. Prince, M. T. Arif, A. Gargoom, M. W. Altaf, I. K. Amin, A. M. T. Oo, K. M. Muttaqi, and M. E. Haque, "Coordinated control of grid-connected PMSG-based wind energy system with STATCOM and supercapacitor energy storage," IEEE Transactions on Industry Applications, vol. 60, no. 3, 2024.
[25] P. K. Kesavan, U. Subramaniam, D. J. Almakhles, and S. Selvam, "Modelling and coordinated control of grid-connected photovoltaic, wind turbine driven PMSG, and energy storage device for a hybrid DC/AC microgrid," Protection and Control of Modern Power Systems, vol. 9, no. 1, 2024.
[26] M. A. Mossa, R. A. Mohamed, and A. S. Al-Sumaiti, "Performance enhancement of a grid-connected wind turbine-based PMSG using effective predictive control algorithm," IEEE Access, vol. 13, 2025.
[27] M. Noman, G. Li, M. W. Khan, K. Wang, and B. Han, "A multi-stage design approach for optimizing a PMSG-based grid-connected ocean wave energy conversion system," Protection and Control of Modern Power Systems, vol. 9, no. 6, 2024.
[28] K. Palanimuthu, G. Mayilsamy, S. R. Lee, S.Y. Jung and Y. H. Joo "Fault Ride-through for PMVG-based Wind Turbine System Using Coordinated Active and Reactive Power Control Strategy," IEEE Trans. on Indus.Electr., 2022.
[29] M. Zhou, W. Wang, X. Li, P. Li, and Y. Chen, “A Coordinated Control Strategy for Black Start of Wind Diesel Storage Microgrid Considering SOC Balance of Energy Storage,” Processes, MDPI, vol. 10, no. 3, pp. 1–19, 2025.
[30] J. Yang, H. Yan, C. Gu, S. Wang, W. Zhao, P. Wheeler and G. Buticchi "Modeling and Stability Enhancement of a Permanent Magnet Synchronous Generator Based DC System for More Electric Aircraft," IEEE Trans. on Indus.Electr., vol. 69, no. 3, pp. 2511-2520, Mar. 2022.
[31] W. Zhang, M. Li, and Q. Chen, “Optimizing Standalone Wind–Solar–Hydrogen Systems: Synergistic Integration of Hybrid Renewables and Multi-Electrolyzer Coordination for Enhanced Green Hydrogen Production,” Processes, vol. 13, no. 12, p. 3801, 2025.

[32] Y. He, Y. Tang, X. Gao, H. Xie, F. Wang, J. Rodriguez, and R. Kennel, "Direct predictive voltage control for grid-connected permanent magnet synchronous generator system," IEEE Transactions on Industrial Electronics, vol. 70, no. 11, 2023.
[33] K. R. Khan, S. Kumar, V. L. Srinivas, R. K. Saket, K. C. Jana, and G. Shankar, "Voltage stabilization control with hybrid renewable power sources in DC microgrid," IEEE Transactions on Industry Applications, vol. 61, no. 2, 2025.
[34] K. Palanimuthu, G. Mayilsamy, S. R. Lee, S. Y. Jung, and Y. H. Joo, "Fault ride-through for PMVG-based wind turbine system using coordinated active and reactive power control strategy," IEEE Transactions on Industrial Electronics, vol. 70, no. 6, 2023.